Journal of Materials Chemistry A

ROYAL SOCIETY OF CHEMISTRY

COMMUNICATION

View Article Online
View Journal

Cite this: DOI: 10.1039/d3ta01658g

Received 20th March 2023
Accepted 22nd May 2023

DOI: 10.1039/d3ta01658g

rsc.li/materials-a

Anisotropic wettability manipulation *via* capturing architected liquid bridge shapes†

Ji Hoon Kim, [a] Jaekyoung Kim,[b] Sohyun Kim,[c] Hyunsik Yoon *[bc] and Won Bo Lee *[a]

Liquid-mediated patterning, which is a fabrication method exploiting the nature of liquids, has achieved great advances in unconventional micro- and nano-fabrication techniques. The easily deformable nature of liquids enables template-based liquid morphing, and the surface tension of the liquid allows for numerous variations of droplet microfluidics. A liquid bridge, which is formed when a droplet of liquid meets two solid surfaces, exhibits the characteristics of both; therefore, it can produce expanded variations in microfabrication and related applications. In this study, liquid bridge-shaped microstructures on a target substrate and template are exhibited. Through the synergy of theoretical investigations and novel construction with elastomeric spacers, the geometry of liquid bridges can be modeled as a function of the solid and liquid properties, separation distance, and morphology of solid surfaces. This study provides various derivatives of structures with tunable sizes, morphologies, and compositions. In particular, the re-entrant morphology of the liquid bridge-shaped microstructures exhibits liquid-repellent characteristics; therefore, it can be exploited for isotropic and anisotropic wettability manipulation. The advances in this research related to semi-confined patterning toward scale-down and controllability unfold a new route for microfabrication, surface engineering, and liquid manipulation.

Introduction

Recent emerging micro- and nano-scale structures for the functionalization of materials rely on the morphing of liquids.[1] Significantly, the variety of morphologies and applications of these liquid-mediated structures is unlimited because they are forms made initially from liquids. For example, liquid droplets[2,3] or jets[4] that are partially constrained or completely unbounded from the substrate have been actively studied through a combination of liquid and substrate compositions; the resulting structures are extensively utilized in optical coding,[5] flexible electronics,[6] and surface engineering.[7] On the other hand, template-based liquid morphing methods utilizing soft templating,[8] transfer printing,[9] and particle replication in non-wetting templates (PRINT)[10] have been developed as derivatives of traditional soft lithography for multifunctional materials. These methods can utilize the confining effect of the template to fabricate complex three-dimensional microstructures for anisotropic wetting[11,12] or shape-tunable functional microparticles for microswimmers,[13] biomedical delivery,[14] and diagnostic applications.[15]

Other emerging techniques include fabrication methods using menisci,[16] which feature intrinsic wet adhesion induced by liquid bridges and enable unconventional fabrications such as liquid-bridge transfer printing[17] and capillary-bridge lithography.[18] Preceding theories of liquid bridges uncovered that the geometry of the liquid bridge and the adhesion force[19–22] induced by the liquid bridge in the equilibrium or dynamic state[23] rely on the properties of the two solid substrates (surface energy, shape, *etc.*), properties of the liquid (viscosity, surface energy, *etc.*), interaction between the solids and liquid (equilibrium/dynamic contact angle and its hysteresis[24,25]), and distance between the two solid surfaces (spacing). The interaction of these theories generates distinctive convex or concave liquid bridges, which are difficult to create with the methods mentioned above; these liquid bridges can be utilized to fabricate functional particles for key–lock assemblies[26] and optical lenses.[27] However, a critical challenge in advancing and scaling down this semi-confined patterning technique is the spacing between solid structures, which is the primary factor determining the shape of the liquid bridge. Therefore, studies utilizing the geometry of liquid bridges at the sub-millimeter scale have not been sufficiently developed.

In this study, we propose an unconventional patterning platform to fabricate an architected liquid bridge-shaped

[a]*Department of Chemical and Biological Engineering, Seoul National University, Seoul 08826, Republic of Korea. E-mail: wblee@snu.ac.kr*

[b]*Department of New Energy Engineering, Seoul National University of Science and Technology, Seoul, 01811, Republic of Korea. E-mail: hsyoon@seoultech.ac.kr*

[c]*Department of Chemical and Biomolecular Engineering, Seoul National University of Science and Technology, Seoul, 01811, Republic of Korea*

† Electronic supplementary information (ESI) available. See DOI: https://doi.org/10.1039/d3ta01658g

microstructure (LBSM) on a target substrate and template. Elastomeric spacers are utilized to exploit the form of stretched liquid bridges, and the dimensions of the resulting LBSMs are systematically controlled by counterbalancing the adhesion force of the liquid bridges with the elastic restoring force of the spacers. The work of adhesion is theoretically investigated to determine whether the LBSM will be transferred to the target substrate or adhere to the stamp. By varying the substrates, stamps, and composition, we demonstrate that various derivatives of LBSMs can be easily fabricated with desired combinations and morphologies. These derivatives of the LBSMs with re-entrant morphology,[28] can be utilized for iso-/anisotropic wettability manipulation. We not only achieve static liquid repellency using discontinuously arranged LBSMs, but also newly design a hierarchical mesh that leverages the liquid bridge shape for directional liquid manipulation. By synergistically utilizing sliding on the re-entrant structure and the mechanism of capillary-driven flow, this mesh can sort liquid droplets depending on surface tension and has the potential for metrology to identify the surface tension of the liquid.

Results and discussion

Fabrication of LBSMs

A schematic of the fabrication process is shown in Fig. 1. First, we employed the direct transfer method to form pre-polymer droplets on the pillar stamp, as shown in Fig. 1a (see also the optical microscopy (OM) images in Fig. S1, ESI†).[29] The shape of the droplets on the pillar was determined based on the equilibrium contact angle (θ_E); perfluoropolyether (PFPE)-urethane methacrylate, which has a low surface energy (~12.7 mN m^{-2}),[30] was utilized as the stamp material to form bulky droplets with high θ_E on the pillars. An SU-8 photoresist was used as the model material for the liquid because its high viscosity is suitable for fabricating manifolds and elaborate microstructures (*e.g.*, those with high aspect ratios), and its high Damköhler number (Da)[31] allows the oxygen inhibition effect on photopolymerization to be neglected. After transferring the pre-polymer droplets to the stamp, a spacer was fabricated on the substrate, as shown in Fig. 1b. Hyperelastic elastomers were employed as spacers owing to their low modulus and restoring force. A weight was used to deform the elastomers such that the droplets were in contact with the substrate, realizing the formation of the liquid bridges.

The liquid bridges were then sculpted and cured, as depicted in Fig. 1c. The solidified LBSMs are attached to both the stamp and the substrate; therefore, the relative magnitudes of the adhesion forces to the stamp and substrate will determine where the resulting structures are fabricated. Ceramics, metals, and metalloids usually have a strong adhesion force with the pre-polymer (low θ_E because of the high surface energy); therefore, the LBSMs can be transferred from the PFPE stamp

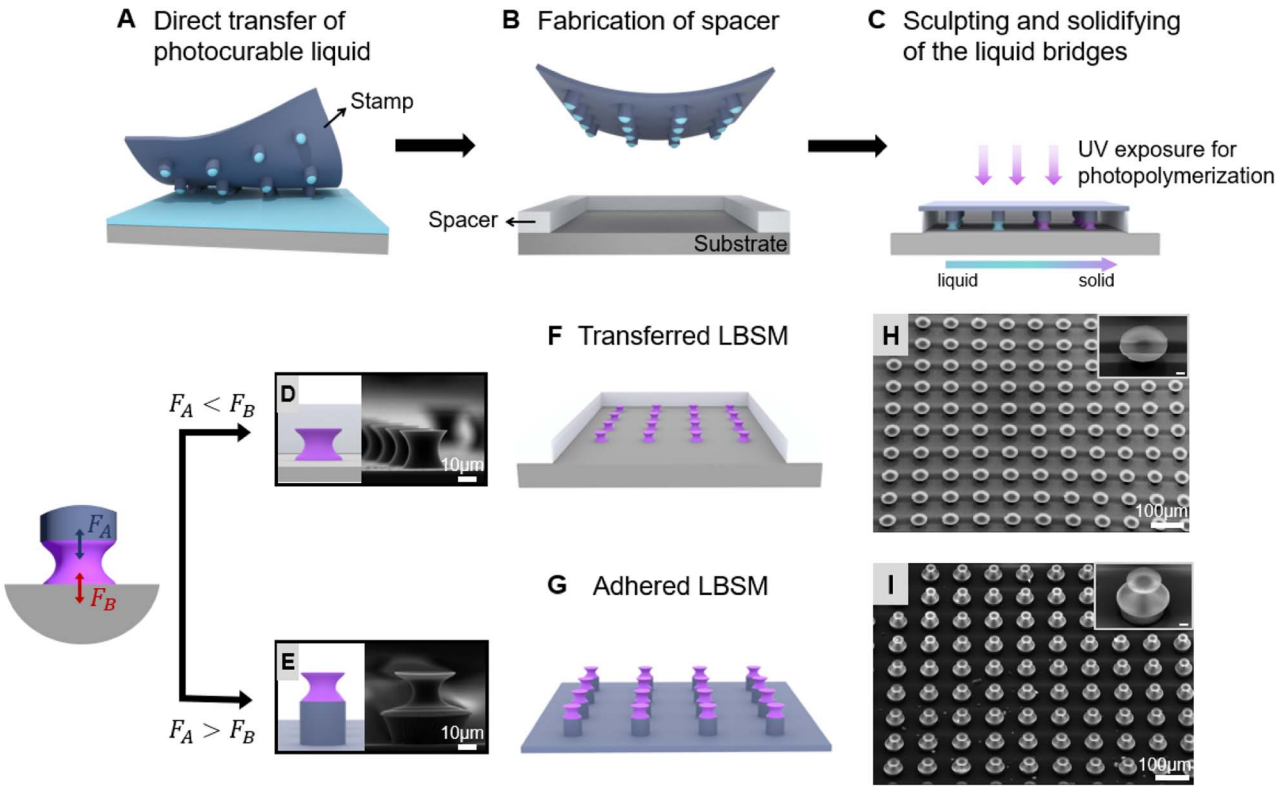

Fig. 1 Schematic diagram illustrating the fabrication procedure of LBSMs: (a) direct transfer of liquid droplets on the protruding micropillars, (b) fabrication of the spacer on the substrate, and (c) sculpting of the LBSMs and adhesion forces acting on the pillar (F_A) and substrate (F_B). Scheme and scanning electron microscopy (SEM) images of the detachment process in the case of (d) $F_A < F_B$ and (e) $F_A > F_B$. Scheme illustrating the LBSMs (f) transferred to the substrate and (g) adhered to the stamp. SEM images of the LBSMs (h) transferred to the substrate and (i) adhered to the stamp. Each inset shows a magnified view. The scale bars of the inset figures are 10 μm.

(Fig. 1d). However, the structures remain on the stamp when a substrate with poor adhesion (higher θ_E on the substrate) is utilized, as illustrated in Fig. 1d.

Architected microfabrication *via* controlled stretching of the liquid bridges on the target structure

To explore the full potential of the architected LBSM, we exploited the geometry of the liquid bridge and designed a force equilibrium-based system. Fig. 2 shows the theoretical investigation and experimental results related to microfabrication *via* controlled stretching and optional transfer of the LBSM. Fig. 2a shows a schematic of the initial state before forming the liquid bridge; the pre-polymer droplet is yet to come into contact with the substrate (to describe the parameters, only one pillar is enlarged and illustrated schematically). When a compressive force is applied under a load of weight, the elastomeric spacers are compressed. If the compressive force exceeds the critical

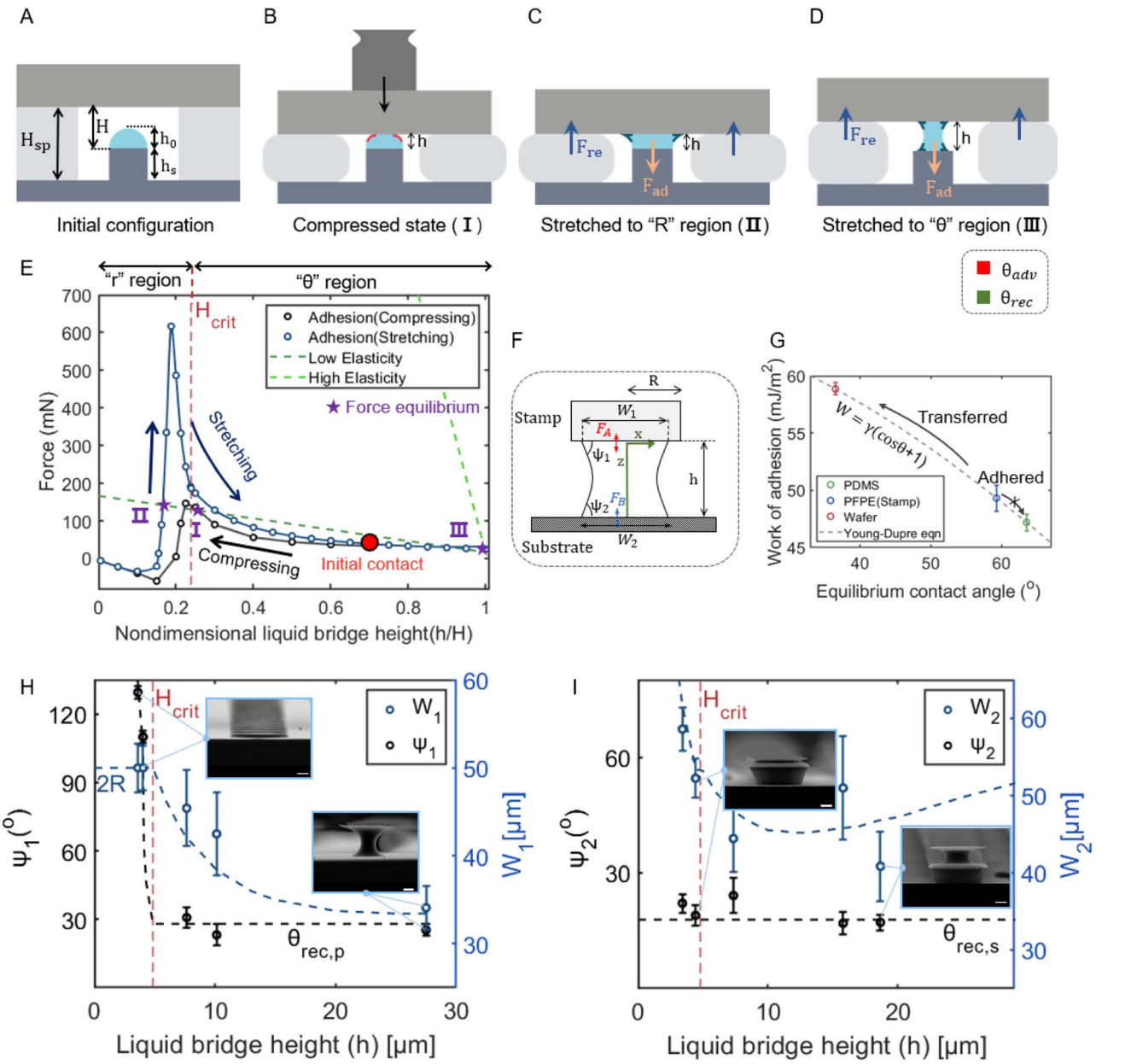

Fig. 2 Architected LBSM fabrication through controlled stretching of liquid bridges with a geometric investigation. (a) Design dimensions of the system before the liquid bridge is formed. Schemes of the liquid bridge (b) in the compressed state, (c) stretched to the "*r*" region, and (d) stretched to the "*θ*" region. (e) Profiles of the adhesion and elastic restoring forces depending on the dimensionless liquid bridge height. Ecoflex ($E \sim 0.1$ MPa) and PDMS ($E \sim 2$ MPa) are employed as elastic spacers. Three states of the liquid bridge are marked with purple stars. (f) Dimensions of the liquid bridge. (g) Work of the adhesion force calculated using the Young–Dupré equation. From the PFPE stamp, the LBSM is transferred to a Si wafer; however, the LBSM adheres to the stamp when the PDMS spacer is utilized. Dimensions of the (h) transferred LBSM and (i) adhered LBSM. Only the dimensions on the upper surface are noted on the graph. SEM images of the liquid bridges in the "*r*" and "*θ*" regions are shown in insets of the graphs. The dotted lines denote theoretical values calculated from governing eqn (6). All scale bars are 10 μm.

force, *i.e.*, $h_0 > H$, a compressed liquid bridge is formed, as illustrated in Fig. 2b. According to the simple 1D linear elastic model,[32] the change in the height of the spacer due to compression, $\Delta H = (H_{sp} - H')$, can be expressed as follows:

$$\Delta H = \frac{mgH_{sp}}{EA} \quad (1)$$

where mg is the gravitational force under a load of weight on a glass slide, E is the elastic modulus of the spacer, and A is the contact area of the spacer.

Once the weight is removed, two different forces act in opposite directions: the restoring force of the elastomer, F_{re}, and the adhesion force of the liquid bridges, F_{ad} (a small gravitational force of ≈16 mN due to the slide glass also acts in the downward direction). According to the linear elastic model, similar to the compressive stage, F_{re}, can be expressed as follows:

$$F_{re} = EA\frac{H - H^*}{H} \quad (2)$$

where H^* is the current state of H. The adhesion force induced by the liquid bridges on the pillars, F_{ad}, has two components:[20] one is induced by the pressure difference between the inside and outside of the meniscus (F_s), and the other is the axial component of the surface tension force (F_c). The total adhesion force acting on a pillar can be expressed as follows:

$$F_{ad,p} = F_{s,p} + F_{c,p} = -\frac{\pi {W_1}^2 \Delta P}{4} + \pi W_1 \gamma_{LV} \sin(\psi_1) \quad (3)$$

where ΔP is the pressure difference between the inside and outside of the liquid bridge, W_1 is the diameter of the wet area on a pillar, γ_{LV} is the surface tension of the liquid, and ψ_1 is the contact angle of the liquid with the pillar, as illustrated in Fig. 2f (the subscript 'p' denotes a force acting on one pillar). Here, ΔP is related to the Young–Laplace equation, which relates the pressure difference to the geometry of the liquid bridge.[33] Moreover, ΔP can be derived using the analytical solution for a capillary bridge between two plates.[22]

$$\Delta P = \gamma_{LV}\left(\frac{1}{R_1} + \frac{1}{R_2}\right) = 4\gamma_{LV}\frac{W_1 \sin(\psi_1) - W_2 \sin(\psi_2)}{{W_1}^2 - {W_2}^2} \quad (4)$$

where R_1 and R_2 are the two principal curvatures of the liquid bridge (details of their derivation are provided in the ESI†). The stamp has numerous pillars ~10^4 cm^{-2}), and the total adhesion force acting on the stamp can be expressed as follows:

$$F_{ad} = F_s + F_c = -\pi n \gamma_{LV}\frac{{W_1}^3 \sin(\psi_1) - {W_1}^2 W_2 \sin(\psi_2)}{{W_1}^2 - {W_2}^2} + \pi n W_1 \gamma_{LV} \sin(\psi_1) \quad (5)$$

where n denotes the number of pillars on the stamp. This equation illustrates that the geometric parameters of the liquid bridge must be known to calculate the adhesion force.

The profile of the liquid bridge in our system is derived by combining the concepts of contact angle hysteresis,[24] the integrated governing equation,[26] and the geometric $r - \theta$ type transition in the fiber–plate system.[21] In this microscale system, the gravitational force of the liquid bridges can be neglected (owing to the small Bond number, $Bo = \Delta\rho g H^2/\gamma_{LV}$). Therefore, when the liquid bridge is in thermodynamic equilibrium, the Laplace pressure is constant. If the geometric relation, Young–Laplace equation, and mean curvature formulation are combined, we can derive an integrated governing equation as follows:

$$2H = \frac{\frac{dz}{dx}}{x\left[1 + \left(\frac{dz}{dx}\right)^2\right]^{1/2}} + \frac{\frac{d^2z}{dx^2}}{\left[1 + \left(\frac{dz}{dx}\right)^2\right]^{3/2}} \quad (6)$$

To solve this equation, we exploit a constraint equation related to volume conservation, which can be expressed as follows:

$$\pi \int_0^h (x(z))^2 dz = V_0 \quad (7)$$

where V_0 refers to the initial volume of the liquid bridge, and h is the height of the liquid bridge.

There are two additional boundary equations related to the contact angle or contact line at the solid/liquid interface in each state. If the liquid bridge is compressed (Fig. 2b), the angle between the substrate and liquid becomes the advancing contact angle. In this case, the contact line is pinned at the stamp/liquid interface; therefore, the boundary conditions can be expressed as follows:

$$X(0) = R \quad (8)$$

$$\left.\frac{dx}{dz}\right|_{z=h} = \tan\left(\frac{\pi}{2} - \theta_{adv,s}\right) \quad (9)$$

For the liquid bridge in the stretched state, two regions with different boundary conditions occur because of the finite size of the pillar: a radius-controlled region and an angle-controlled region (hereafter referred to as the "r" region and "θ" region).

If the height of the liquid bridge is smaller than the critical height (Fig. 2c), the contact line is pinned at the stamp/liquid interface, similar to the compressed state. In this case, the angle between the substrate and liquid becomes a receding contact angle. Therefore, the boundary conditions are given by using eqn (8) and

$$\left.\frac{dx}{dz}\right|_{z=h} = \tan\left(\frac{\pi}{2} - \theta_{rec,s}\right) \quad (10)$$

If the liquid bridge is stretched beyond the value of H_{crit}, the contact line deviates from the pinned state, and the angles between the two solid surfaces and the liquid both satisfy the receding contact angle condition (Fig. 2d). Therefore, the boundary conditions are given by using eqn (10) and

$$\left.\frac{dx}{dz}\right|_{z=0} = \tan\left(\frac{\pi}{2} - \theta_{rec,p}\right) \quad (11)$$

From these equations, it can easily be inferred that H_{crit} is the value of H that satisfies both the contact line pinning and

contact angle conditions (details of the derivation are provided in the ESI†).

Accordingly, after obtaining a liquid bridge profile that satisfies each boundary condition in the form of $x = x(z)$, F_{ad} can be calculated as shown in Fig. 2e. The height of the liquid bridges is expressed as a dimensionless value, h/H. In the compressed state, the adhesion force gradually increases in the early stage as the increase in $\sin(\psi_1)$ results in an increase in $F_{c,p}$. However, as the shape of the liquid bridges changes from concave to convex, ΔP becomes a positive value; accordingly, F_{ad} decreases sharply and becomes a negative value. In contrast, as the weight is removed and stretching of the liquid bridges begins, the liquid bridges return to a concave shape. As h increases during the stretching process, ψ_1 changes from an obtuse angle to an acute angle, and F_{ad} reaches a maximum value in the "r" region. In the subsequent stretching process, as ψ_1 converges to $\theta_{rec,p}$, the curvature of the liquid bridges decreases steadily, and F_{ad} gradually decreases.

In addition to F_{ad}, F_{re} is also expressed in Fig. 2e. From eqn (2), the slope of F_{ad} is $-(EA)$. Therefore, condition A is fixed and the slope is proportional to E. We utilized two types of elastomers, Ecoflex ($E \sim 0.1$ MPa) and polydimethylsiloxane (PDMS; $E \sim 2$ MPa); the two F_{ad} are shown as a dark green line and light green line, respectively, in Fig. 2e. In the case of a small F_{ad} (dark green line), the liquid bridges are pinned in the "r" region because a force equilibrium is formed at point C, as illustrated in Fig. 2c. However, in the case of the larger F_{ad}, no force equilibrium is formed until point D, and the liquid bridges are stretched to the "θ" region, as illustrated in Fig. 2d.

To investigate whether the solidified microstructures are transferred to the substrate or adhere to the stamp, we employed the Young–Dupré equation[34] to describe the work of adhesion (note: the work of adhesion at the solid/solidified liquid interface is different from the adhesion force induced by the liquid bridge), as follows:

$$W = \gamma_{LV}(\cos\theta + 1) \tag{12}$$

where W is the work of adhesion, and θ is the contact angle at the liquid/solid interface.

To calculate W, the equilibrium contact angles of the prepolymer on the substrates were measured, and the results are plotted in Fig. 2g. The adherence of LBSM to the stamp and its transfer to the new substrate are determined by the criteria of work of adhesion, as follows:

$$W_1^2 W_{p-l} > W_2^2 W_{s-l} \text{ Adhered to stamp} \tag{13}$$

$$W_1^2 W_{p-l} < W_2^2 W_{s-l} \text{ Transferred to substrate} \tag{14}$$

where W_{p-l} is the work of adhesion at the pillar/liquid interface, and W_{s-l} is the work of adhesion at the substrate/liquid interface.

By controlling the profile of the liquid bridges and exploiting the difference in the work of adhesion, we systematically obtained transferred structures, as shown in Fig. 2h, and adhered structures, as shown in Fig. 2i (consecutive SEM images are shown in Fig. S2, ESI†). Only those values on the upper surface are displayed as y-axis values. The dotted lines denote the theoretical values calculated from eqn (6) and the boundary conditions (BCs) at each height. In the case of the transferred structures, the taper angles on the upper surface (ψ_1) vary with h in the "r" region, and the upper diameter, W_1, is fixed at $2R$ because of the contact-line pinning of the liquid on the pillar side. However, as it enters the "θ" region, ψ_1 converges to $\theta_{rec,p}$, and W_1 decrease as h increases. However, in the case of the adhered structures, the taper angles on the upper surface (ψ_2) have a constant value, $\theta_{rec,s}$, because they always exist as a boundary condition in the stretching process. Owing to volume conservation, the upper surface diameter (W_2) decreases as h increases in the early stretching stage. As it enters the "θ" region, W_2 increases again to satisfy the receding angle BCs.

The dimensional range of a LBSM can be determined by two scenarios. The first scenario involves the breakup of the liquid bridge during the stretching process, while the second scenario pertains to the fracture of the solidified structure, particularly in the neck region, induced by stress during the detachment processes. In our research, the building material, SU-8 3050, exhibits resistance to breakup during the stretching process, thereby facilitating the attainment of aspect ratios (neck-to-height ratios) exceeding 100.[35] Consequently, fractures occurring during the detachment process are considered to be the primary cause of the "disabled" LBSM in this fabrication process. Based on experimental measurements, the critical neck-to-height ratio for defect-free formation of a large-area LBSM is approximately 3. Therefore, for a stamp with $D = 50$ μm, the critical height is estimated to be around 30 μm (Fig. S3, ESI†).

Derivatives of LBSMs

A liquid bridge can be formed between various solid structures, not just between bare flat surfaces. Therefore, by exploiting the tunability of the substrate, stamp, and composition, numerous LBSM derivatives can be fabricated. By employing a curved substrate (Fig. 3a), 1D curved structures (Fig. 3b) and 2D curved structures (Fig. 3c) were fabricated on the stamp. Similarly, patterned substrates can also be utilized for multiscale hierarchical structures (Fig. 3d), resulting in wrinkled (Fig. 3e) and stripped (Fig. 3f) patterns on the top of the LBSM. In addition to transferring macroscopic curves and nanoscale morphologies onto the microstructure, our fabrication method allows for the transfer of micropatterns of comparable scale onto the LBSM, resulting in an LBSM with prism-shaped tips (Fig. S4, ESI†).

Furthermore, our fabrication method offers the flexibility to utilize various other types of stamps for the transfer process Although the direct transfer step poses several challenges associated with Rayleigh–Plateau instability,[36] we effectively addressed this issue by utilizing discontinuous dewetting (DD)[37] to intentionally split droplets. Additionally, for the line stamp, we carefully manipulated various factors such as the spin-coating condition and geometry of the line pattern to successfully fabricate integrated half-cylindrical line features. Through these manipulations, linear LBSMs (Fig. 3g) and pyramidal

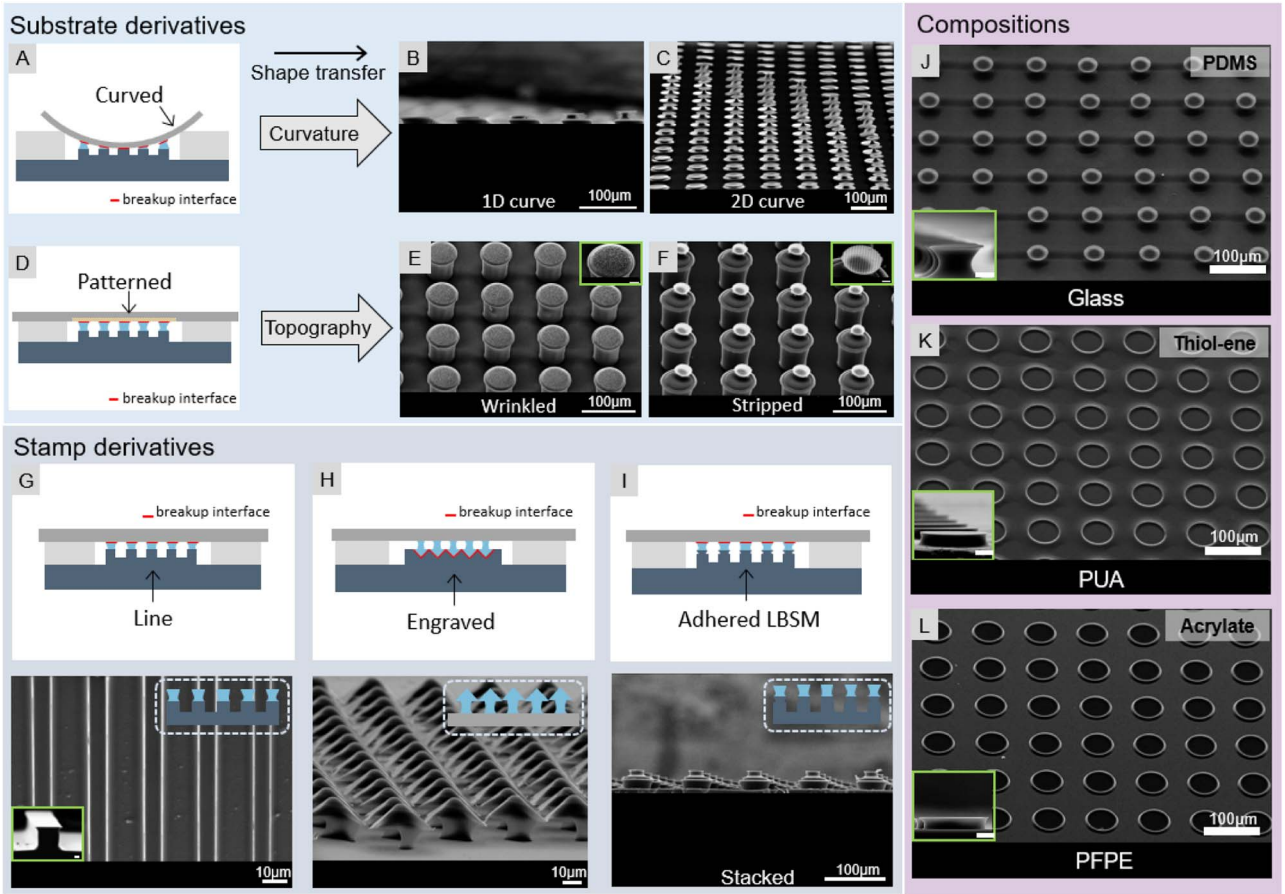

Fig. 3 Miscellaneous derivatives of LBSMs obtained by varying the substrate, stamp, and composition. (a) Scheme for the fabrication of curved LBSMs utilizing a curved substrate. SEM images of LBSMs with (b) one-dimensional and (c) two-dimensional curvatures. (d) Scheme for the fabrication of multiscale LBSMs utilizing micro/nanopatterned substrates. SEM images of adhered LBSMs with (e) micro-wrinkled and (f) nano-stripped surfaces. The inset images show magnified views. (g) SEM image of linear LBSMs fabricated using a line-patterned stamp. The inset image shows a cross-section of the LBSM. (h) SEM image of LBSMs fabricated using a negative pyramidal stamp. Discontinuous dewetting (DD) is used to form discontinuous liquid droplets on each microwell. (i) Scheme and SEM image of stacked LBSMs. Tri-layered LBSMs are fabricated using adhered LBSMs as the stamp. Various compositions are employed to transfer the LBSMs to the target substrate. (j) Silicon rubber (PDMS) LBSMs on a glass substrate, (k) thiol–ene LBSMs on a PDMS substrate, and (l) acrylate LBSMs on a PFPE substrate are shown as model compositions. All scale bars of the inset figures are 10 μm.

LBSMs (Fig. 3h, fabrication procedure in Fig. S5†) were fabricated on the target substrates. To demonstrate the various material combinations possible with this system, we used different materials for the stamp, LBSM, and substrate. In addition to showcasing the variation of stamp materials (as shown in Fig. S6†), we successfully produced LBSMs made of PDMS (thermocuring), thiol–ene, and acrylate on glass, acrylate, and PFPE substrates, respectively (as shown in Fig. 3j–l). This diversity of compositions demonstrates that LBSMs can be fabricated from a range of desirable materials and transferred onto various target substrates, including flexible ones.

Isotropic/anisotropic wettability manipulation through LBSMs

Miscellaneous LBSM derivatives provide unexpected opportunities to manipulate static and dynamic wettability because correlated independent factors can provide synergism between various morphologies and hybrid materials. In this study, we demonstrate wettability manipulation by fabricating an array of LBSMs over a large area. By transferring the LBSMs to the target substrate, we can modulate the target substrate to create amphiphilic (θ_E < 90°) or super-amphiphobic (θ_E ~150°) surfaces, as shown in Fig. 4b. When LBSMs in the "*r*" region are transferred to the substrate, the taper angle is larger than the equilibrium contact angle (θ_E) on the bare SU-8 surface. Therefore, the apparent contact angle (θ^*) satisfies the Cassie–Baxter relation, and the liquids are partially wetted on the rough composite surface.[38] Meanwhile, as the liquid bridges are further stretched to the "θ" region, the taper angle converges to $\theta_{rec,s}$. Accordingly, these surfaces repel liquids with θ_E that are larger than the taper angle through the air-trapping mechanism. However, when θ_E of the liquid is smaller than the taper angle (*e.g.*, θ_E of hexadecane ~19°), the liquid is partially wetted, similar to the LBSMs in the "*r*" region. To provide evidence that the LBSMs demonstrate minimal lateral pinning of droplets[39] and do not leave a microscopic liquid residue[40,41] without

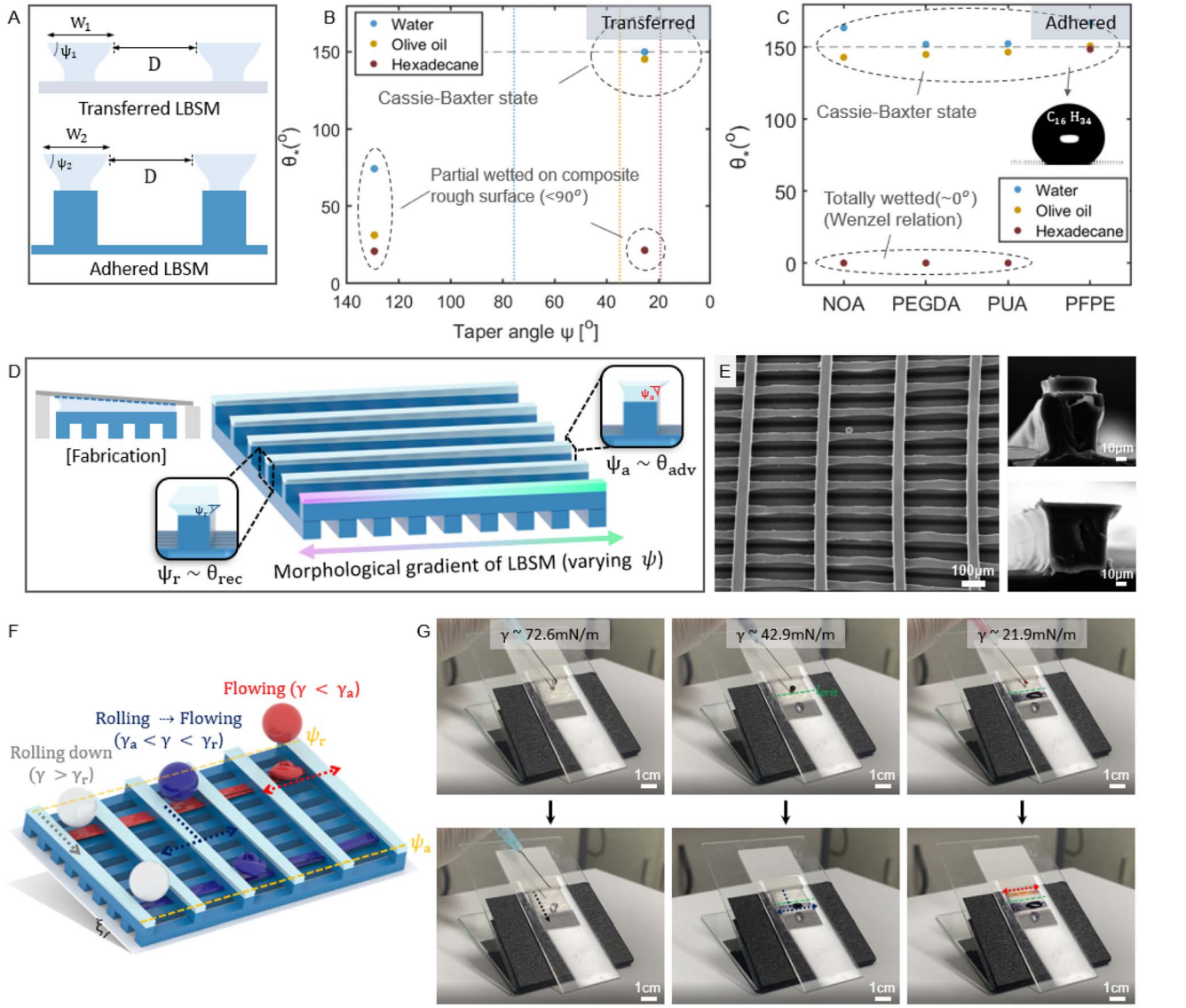

Fig. 4 Isotropic/anisotropic wettability manipulation through LBSMs. (a) Scheme of the dimensions of transferred/adhered LBSMs. (b) Measured apparent contact angles (θ^*) of transferred LBSMs with varying taper angles. The vertical dotted lines indicate the equilibrium contact angles of liquids on the bare SU-8 surface. (c) Measured apparent contact angles (θ^*) of adhered LBSMs with varying structural materials. Double replica molding is employed to fabricate LBSMs adhered to various materials. The inset shows a hexadecane droplet in the Cassie state on the LBSM. (d) Design for fabricating a hierarchical mesh with a morphological gradient of a LBSM. Spacers of varying heights are used to fabricate the mesh. The variation in LBSM morphology accompanies the variation of the taper angle (ψ), which ranges from ψ_r ~20° to ψ_a ~78°. (e) SEM images of the hierarchical mesh with a gradient. A 45° tilted view and cross-sectional view of a gradient LBSM with ψ_a (up) and ψ_r (bottom) are displayed. (f) Design to demonstrate the sorting of liquids and the use of metrology to determine surface tension through the mesh. (g) Photographs showcase the movement of liquid droplets with different surface tensions. A droplet with high surface tension ($\gamma = 72.6$ mN m^{-1} > γ_r) rolls down along the upper lines. Meanwhile, a droplet with moderate surface tension ($\gamma_a = 42.9$ mN m^{-1} > γ_r) undergoes a distinct transition from rolling along the upper lines to capillary-driven flowing along the lower lines, which are oriented perpendicular to the upper lines. A droplet with low surface tension ($\gamma_a = 21.9$ mN m^{-1} > γ_a) directly flows in the perpendicular direction along the lower lines. The green dot lines represent the transition from rolling to flowing for a liquid with a surface tension of 42.9 mN m^{-1}.

additional slippery coatings for the Cassie state with the air-trapping mechanism, dynamic contact angles on LBSMs consisting of SU-8 and PUA (utilized for anisotropic liquid manipulation as described below) were measured and compared with those of PDMS, which is commonly used as the control material for superhydrophobic surfaces (Fig. S7 and Movie S2–S4†).

The adhered LBSM, which can be utilized as an integrated new stamp, can be fabricated through double replica molding using soft lithography. This enables the fabrication of adhered LBSMs of the desired materials (Fig. 4c). This adhered LBSM features the same taper angle (θ_{rec} on the PDMS substrate); therefore, the apparent contact angle (θ^*) has almost the same value regardless of the liquid bridge height. Here, we selected

the adhered LBSM in the "θ" region as the model structure. In this case as well, the taper angle *vs.* θ_E is the criterion for wetting, and thus liquids are wetted only if θ_E is smaller than the taper angle (hexadecane on Norland optical adhesives (NOA), poly(ethylene glycol) diacrylate (PEGDA), and polyurethane acrylate (PUA) patterns). Notably, compared to the transferred LBSMs, the whole structure consists of one material; liquids are completely wetted on the adhered LBSMs in the impregnating case, which is in accordance with Wenzel's relation.[7] The θ_E of hexadecane on the PFPE substrate is the largest among the liquids used ($\theta_E \sim 36°$), and thus it exhibits superior liquid–repellent properties (the calculation of the solid fraction is shown in Fig. S8† and the measured/estimated contact angles are listed in Tables S1 and Table S2, ESI†).

In addition to the static wettability manipulation of liquids, LBSMs can provide dynamic wettability control through a LBSM -induced functional mesh for directional transport of liquids. As a first step, rectilinear lines were transferred to a line-patterned substrate arranged perpendicularly. Then, using spacers of varying heights, a hierarchical mesh with a linear gradient adhered LBSM was fabricated, as illustrated in Fig. 4d. The linearly varying height of the liquid bridge allows for a continuous variation of ψ from the θ_{rec} to θ_{adv} of PUA on the PDMS substrate, which is used as the building liquid and substrate for the hierarchical mesh. The mesh structure was characterized using SEM images, as shown in Fig. 4e, which displayed a 45° tilted view and cross-sectional views of the LBSM with $\psi_a \sim \theta_{adv} \sim 78°$ (up) and $\psi_r \sim \theta_{rec} \sim 20°$ (bottom). Given that the solid–gas and liquid–gas interfacial tensions remained constant within the experimental system, the critical surface tensions, denoted as γ_r and γ_a, were defined as the thresholds for distinguishing the Cassie state with air-trapping and the Cassie state with impregnation at regions with local taper angles of ψ_r and ψ_a, respectively. The synergistic combination of capillary flow and slipping on the re-entrant structure enables the mesh to be utilized for sorting of liquids by surface tension, as illustrated in Fig. 4f. A droplet with high γ, such as deionized water ($\gamma \sim 72.6$ mN m; θ_E on PUA $\sim 92°$), rolls down along the tilted direction. Meanwhile, when we dropped a droplet with moderate γ on a region with local taper angle ψ_r (a mixture of deionized water and ethanol in a 4 : 1 ratio; $\gamma \sim 42.9$ mN m; θ_E on PUA $\sim 59°$), the results indicated that the droplet rolled on regions of the surface along the upper lines where $\psi < \theta_E$, while the droplet penetrated and flowed along the lower lines which are set in the perpendicular direction[42] where $\psi > \theta_E$. Similarly, a liquid droplet with low γ (ethanol; $\gamma \sim 21.9$ mN m; θ_E on PUA $\sim 11°$) directly flowed along the lower lines, because the local ψ was always larger than θ_E. Fig. 4g and Movie S1† demonstrate three different mechanisms of liquid manipulation for sorting liquid by surface tension. This functional mesh can not only be utilized for sorting of liquids by surface tension, but also has potential for metrology to identify γ (or θ_E) of a liquid by observing the transition point from rolling to flowing of the liquid droplet. In this case, droplets with moderate γ begin to collapse 65% points from the starting point with ψ_r. Assuming a linear variation of ψ from ψ_r (20°) to ψ_a(78°), the ψ near the transition point can be estimated to be approximately 58°, which is agreement with the measured θ_E on the PUA substrate ($\sim 60°$).

Experimental section

Materials

The photoresist SU-8 3050 was purchased from MicroChem. An acrylate-based oligomer (PUA 301) was purchased from Material Chemicals Network Co., Ltd, and used as received. PFPE-urethane methacrylate (MD700) was purchased from JUNSUNG Polymer Co., Ltd and prepared by mixing with the photoinitiator 2-hydroxy-2-methylpropiophenone (5 wt%, Darocur 1173, Sigma-Aldrich) The hydrogel PEGDA (M_w: 700 g mol^{-1}) was purchased from Sigma-Aldrich, USA, and prepared by mixing with the photoinitiator 2,2-dimethoxy-2-phenylacetophenone (5 wt%, Irgacure 651, Sigma-Aldrich). The thiol–ene-based adhesive, NOA 81, was purchased from Norland Products and used as received. A Sylgard 184 PDMS elastomer kit was purchased from Dow Corning, and Ecoflex 00-30 was purchased from Smooth-on Inc., USA. Slide glass (Marienfeld/Superior, Germany) and silicon wafers (iCell Co., Ltd) were employed as the backplane and substrate, respectively. 3-(Trimethoxysilyl)propyl methacrylate (Sigma-Aldrich) was used to enhance the adhesion between the glass and the cured pattern. Photopolymerization was performed at room temperature using a Fusion Cure 360 (MINUTA Tech, Republic of Korea) with a light intensity of 5.0 mW cm^{-2}.

Characterization

Optical microscopy (Olympus BX41M) and an EM-30 scanning electron microscope (COXEM, Republic of Korea) with an acceleration voltage of 10 kV were employed to obtain the OM and SEM images, respectively.

Contact angle measurement

Contact angle images were obtained using a contact angle meter (CAM 200, KSV Instrument Ltd, Finland). The contact angles were measured using the built-in software of the contact angle meter or ImageJ software.

Fabrication of liquid bridge-mediated microstructures

A stamp containing pre-polymer droplets was placed on the substrate with an elastomeric spacer. Regardless of the initial contact between the droplets and substrate in this step, gravitational force was applied by increasing the weight applied to the top of the stamp for 60 s. Subsequently, the weight was removed to allow for stretching of the liquid bridges. A stabilization time of approximately 10 min allowed the liquid bridges to achieve the equilibrium shape. After stabilization, UV irradiation was applied for 5 min. We slightly detached the LBSMs after curing, and then the microstructures were adhered to the stamp or transferred to the substrate, depending on the difference in the adhesion forces of the two sides. To enhance the adhesion strength at the stamp/solidified liquid bridge interfaces, the microstructures were exposed to additional UV light for 30 min.

Further experimental and theoretical investigations can be found in the ESI.†

Conclusions

As an advancement in the morphing of interfacial liquids, we developed an innovative platform for fabricating LBSMs over a large area. Utilizing abundant theoretical investigations (*e.g.*, the geometry of the liquid bridge, force equilibrium-based systems, and the Young–Dupré equation) we systematically fabricated size/shape-tunable LBSMs on the target substrate. Miscellaneous LBSM derivatives were obtained by varying the stamps, substrates, and composition. The ability of LBSMs to be transferred to the desired substrate (*e.g.*, desired composition and flexibility) and readily replicated using soft lithography expands the availability of LBSMs. Inspired by the unique curve and re-entrant form of the liquid bridge, LBSMs were utilized to realize isotropic/anisotropic wettability manipulation of liquids. By modulating the geometry of the liquid bridge, amphiphilic (θ_E < 90°) or super-amphiphobic (θ_E ~150°) surfaces could be fabricated by controlling the composition and spacing. Beyond static wettability control, the proposed functional mesh, incorporating a morphological gradient on an LBSM, has the ability to sort liquids based on their surface tension. The combination of capillary flow and rolling mechanisms on the LBSM enhances its potential for smart liquid manipulation and identifying liquid properties through metrologic calculations, extending its application. While this research solely demonstrates the liquid sorting process using our novel fabrication method, the diverse morphological derivatives depicted in Fig. 3 offer the potential for additional functionalities within the underlying re-entrant structure. For instance, in the case of a curved LBSM (Fig. 3a–c), the transfer of curvature to the array enables directionality, thereby presenting possibilities such as water collection. Furthermore, the adoption of an engraved stamp in creating a LBSM (Fig. 3h) showcases a double re-entrant structure, leading to enhanced liquid repellency. Additionally, the stacking of LBSMs, as illustrated in Fig. 3i, can enhance stability and robustness for amphiphobic surfaces.

Amid the plethora of micro/nanofabrication methods for fabricating re-entrant structures,[43] our approach stands out by virtue of its incorporation of the benefits of prior template molding methods[43] and its unique strengths in the realm of morphological and compositional versatility (a comparison of our fabrication method with others is presented in Table S3,† which was reprinted from ref. [43] with minor revisions). We contend that the myriad material and morphological combinations achievable *via* our technique harbor tremendous potential to serve as a platform for comprehensive surface engineering such as self-cleaning and smart liquid manipulation, representing a valuable alternative to conventional methodologies.

Author contributions

Ji Hoon Kim: conceptualization, methodology, investigation, data curation, writing – original draft. Jaekyoung Kim: visualization, investigation. Sohyun Kim: investigation. Hyunsik Yoon: funding acquisition, project administration, validation, supervision, writing – review & editing. Won Bo Lee: funding acquisition, project administration, validation, writing – review & editing.

Conflicts of interest

The authors declare no conflict of interest.

Acknowledgements

This study was financially supported by the National Research Foundation of Korea (NRF) [grant numbers NRF-2018M3D1A1058633, and NRF-2021M3H4A6A01041234] and Technology Innovation Program (20010371) funded by the Ministry of Trade, Industry & Energy (MOTIE, Korea).

Notes and references

1 J. Bae, J. Lee, Q. Zhou and T. Kim, *Adv. Mater.*, 2019, **31**, 1804953.
2 X. Fang, J. Shi, X. Zhang, X. Ren, B. Lu, W. Deng, J. Jie and X. Zhang, *Adv. Funct. Mater.*, 2021, **31**, 2100237.
3 X. Li, B. Hu, M. Zhang, X. Wang, L. Chen, A. Wang, Y. Wang, Z. Du, L. Jiang and H. Liu, *Adv. Mater.*, 2019, **31**, 1904610.
4 T. Jiang, Y. Qiao, W. Ruan, D. Zhang, Q. Yang, G. Wang, Q. Chen, F. Zhu, J. Yin and Y. Zou, *Adv. Mater.*, 2021, **33**, 2104779.
5 Y. Liu, F. Li, L. Qiu, K. Yang, Q. Li, X. Zheng, H. Hu, T. Guo, C. Wu and T. W. Kim, *ACS Nano*, 2019, **13**, 2042–2049.
6 D. Li, W. Y. Lai, Y. Z. Zhang and W. Huang, *Adv. Mater.*, 2018, **30**, 1704738.
7 J. Chi, X. Zhang, Y. Wang, C. Shao, L. Shang and Y. Zhao, *Mater. Horiz.*, 2021, **8**, 124–144.
8 H. Lee, Y. Ji Seo, J. Kim, M. Jun Bae, S. Hwang, J. Gun Bae, W. Bo Lee and H. Yoon, *J. Chem. Eng.*, 2022, **434**, 134665.
9 K. Kim, B. Kim and C. H. Lee, *Adv. Mater.*, 2020, **32**, 1902051.
10 A. C. Misra and J. Lahann, *Adv. Healthcare Mater.*, 2018, **7**, 1701319.
11 P. Ge, S. Wang, J. Zhang and B. Yang, *Mater. Horiz.*, 2020, **7**, 2566–2595.
12 H. Geng, H. Bai, Y. Fan, S. Wang, T. Ba, C. Yu, M. Cao and L. Jiang, *Mater. Horiz.*, 2018, **5**, 303–308.
13 P. Sharan, A. Nsamela, S. C. Lesher-Pérez and J. Simmchen, *Small*, 2021, **17**, 2007403.
14 W. Li, L. Zhang, X. Ge, B. Xu, W. Zhang, L. Qu, C.-H. Choi, J. Xu, A. Zhang, H. Lee and D. A. Weitz, *Chem. Soc. Rev.*, 2018, **47**, 5646–5683.
15 A. Choi, K. D. Seo, D. W. Kim, B. C. Kim and D. S. Kim, *Lab Chip*, 2017, **17**, 591–613.
16 J. Kim, Y. Ryu, C. H. Kim, S. G. Heo, K.-Y. Yoo and H. Yoon, *Adv. Funct. Mater.*, 2021, **31**, 2010053.
17 A. Corletto and J. G. Shapter, *ACS Appl. Nano Mater.*, 2020, **3**, 8148–8160.
18 J. Feng, X. Jiang, X. Yan, Y. Wu, B. Su, H. Fu, J. Yao and L. Jiang, *Adv. Mater.*, 2017, **29**, 1603652.
19 E. B. Dussan, *Annu. Rev. Fluid. Mech.*, 1979, **11**, 371–400.

20 F. M. Orr, L. E. Scriven and A. P. Rivas, *J. Fluid Mech.*, 1975, **67**, 723–742.
21 J. Qian and H. Gao, *Acta Biomater.*, 2006, **2**, 51–58.
22 Y. Wang, S. Michielsen and H. J. Lee, *Langmuir*, 2013, **29**, 11028–11037.
23 O. Pitois, P. Moucheront and X. Chateau, *J. Colloid Interface Sci.*, 2000, **231**, 26–31.
24 H. Chen, A. Amirfazli and T. Tang, *Langmuir*, 2013, **29**, 3310–3319.
25 E. J. De Souza, L. Gao, T. J. McCarthy, E. Arzt and A. J. Crosby, *Langmuir*, 2008, **24**, 1391–1396.
26 L. Wang, M. Qiu, Q. Yang, Y. Li, G. Huang, M. Lin, T. J. Lu and F. Xu, *ACS Appl. Mater. Interfaces*, 2015, **7**, 10727–10733.
27 L. Wang and T. J. McCarthy, *Proc. Natl. Acad. Sci. U. S. A.*, 2015, **112**, 2664–2669.
28 A. Tuteja, W. Choi, M. Ma, J. M. Mabry, S. A. Mazzella, G. C. Rutledge, G. H. McKinley and R. E. Cohen, *Science*, 2007, **318**(5856), 1618–1622.
29 D. Kang, C. Pang, S. M. Kim, H. S. Cho, H. S. Um, Y. W. Choi and K. Y. Suh, *Adv. Mater.*, 2012, **24**, 1709–1715.
30 H. Cho, J. Kim, H. Park, J. Won Bang, M. Seop Hyun, Y. Bae, L. Ha, D. Yoon Kim, S. Min Kang, T. Jung Park, S. Seo, M. Choi and K.-Y. Suh, *Nat. Commun.*, 2014, **5**, 3137.
31 D. Dendukuri, P. Panda, R. Haghgooie, J. M. Kim, T. A. Hatton and P. S. Doyle, *Macromolecules*, 2008, **41**, 8547–8556.
32 L. D. Landau, *Theory of Elasticity*, Pergamon, London, 1959.
33 A. W. Adamson, *Physical Chemistry of Surfaces*, Wiley, New York, 3rd edn, 1976.
34 M. E. Schrader, *Langmuir*, 1995, **11**, 3585–3589.
35 K. Lee, H. C. Lee, D. S. Lee and H. Jung, *Adv. Mater.*, 2010, **22**, 483–486.
36 I. Kim and D. Y. Khang, *J. Appl. Polym. Sci.*, 2017, **134**, 45028.
37 H. U. Kim, Y. H. Roh, S. J. Mun and K. W. Bong, *ACS Appl. Mater. Interfaces*, 2020, **12**, 53318–53327.
38 P.-G. d. Gennes, *Capillarity and Wetting Phenomena: Drops, Bubbles, Pearls, Waves*, Springer, New York, 2004.
39 X. Li, J. Yang, K. Lv, P. Papadopoulos, J. Sun, D. Wang, Y. Zhao, L. Chen, D. Wang, Z. Wang and X. Deng, *Natl. Sci. Rev.*, 2021, **8**, nwaa153.
40 S. Huang, J. Li, L. Liu, L. Zhou and X. Tian, *Adv. Mater.*, 2019, **31**, 1901417.
41 S. M. Kang and J. H. An, *ACS Appl. Mater. Interfaces*, 2022, **14**, 39646–39653.
42 Y. Chen, L. S. Melvin, S. Rodriguez, D. Bell and M. M. Weislogel, *Microelectron. Eng.*, 2009, **86**, 1317–1320.
43 H. H. Vu, N. T. Nguyen and N. Kashaninejad, *Adv. Mater. Technol.*, 2023, 2201836.

